Structure and Stoichiometry Self-Organization in a Mixed Vanadium–Iron Oxide Honeycomb Film on Ru(0001)

Piotr Igor Wemhoff, Claudine Noguera, Jacek Goniakowski, Niklas Nilius

Structure and Stoichiometry Self-Organization in a Mixed Vanadium-Iron Oxide Honeycomb Film on Ru(0001)

Piotr Igor Wemhoff, [a] Claudine Noguera,[b] Jacek Goniakowski,[b,*] and Niklas Nilius [a,*]

[a] Carl von Ossietzky Universität Oldenburg, Institut für Physik, D-26111 Oldenburg, Germany

[b] CNRS-Sorbonne Université, Institut des Nanosciences de Paris, UMR 7588, F-75005 Paris, France

Abstract

We report successful synthesis of a mixed V/Fe ultra-thin oxide phase on Ru(0001), in which mixing is governed by a self-organization scheme that selects V/Fe compositions close to 50%. Bias-dependent high resolution STM imaging and DFT simulations enabled a thorough characterization of its honeycomb-like structure with additional oxygen anions at the metal/oxide interface, as well as a convincing assignment of the two observed defect types. The mixed layer displays a unique structure and stoichiometry intermediate between those of pure vanadium and iron oxide films under the same experimental conditions. It results from a singular, geometry-driven mixing scenario in 2D which, thanks to the high interfacial oxygen content, is reminiscent of that known for bulk ternary oxides. Comparison with V/Fe mixed honeycomb layers on Pt(111) exemplifies how the choice of the metal substrate may induce largely different mixing behaviors. Such versatility opens a way towards a thorough fundamental understanding of the principles that underlie oxide alloying in 2D.

1. Introduction

Ternary and quaternary mixed oxides are omnipresent in all major fields of science and technology, in particular, in heterogeneous catalysis, photovoltaics, microelectronics and superconductivity.[1,2,3,4] A striking advantage is their compositional flexibility that offers new degrees of freedom to install desired structural, electronic and optical properties, being not accessible to binary oxides. The mutual coupling between the lattice cations hereby controls the character of the oxygen network, the occurrence of internal charge-transfer processes, the position of valence and conduction band, and the overall reducibility hence the chemical activity of the material. In the 3D limit, ternary and quaternary oxides crystallize in well-

defined lattice structures and stoichiometries that are typically governed by the radii of the involved cations, their charge state, and the degree of covalency of their binding.[5] Perovskite oxides, for example, adopt trigonal, orthorhombic, cubic and hexagonal crystal symmetries, depending on the size difference between corner and central cations.[6] Similarly, the deviation of spinel unit cells from perfect cubic symmetry is largely controlled by the electronegativity of the involved cations.[7] In general, the building principles and ion distributions in mixed oxide materials are well understood in the bulk limit.

The situation changes markedly in mixed oxides with 2D character. The absence of layers above and below the film strongly reduces the oxide Madelung potential, which in turn changes the size of the band gap. Moreover, the dielectric nature of the environment, i.e., of gas phase and substrate above and below the film, affects the screening response of the oxide ions. This variability is, to a good portion, responsible for the compelling properties of layered dichalcogenide materials,[8] but applies to 2D mixed oxides in similar manner. Finally, pronounced interfacial coupling may alter geometry and charge configuration of 2D oxide lattices, often with dramatic consequences on their electronic structure and surface composition.[9,10] Cationic ordering in 2D mixed oxides may thus deviate from the one in bulk systems, with severe effects on their functionality.

Several examples in the literature corroborate this conclusion. While Co and Fe are immiscible in the bulk, oxide films with variable Co/Fe ratios and unexpected hydroxylation properties can be prepared on an Au(111) support.[11] The structure and stoichiometry of 2D tungsten bronzes ($CuWO_3$, $NaWO_3$, $FeWO_3$) were found to deviate strongly from their 3D analogues.[12,13] While Mo and Ca crystallize in powellite ($CaMoO_4$) and perovskite structures ($CaMoO_3$) in the bulk, a number of specific 2D phases could be stabilized on Mo(001).[14] Ultrathin Fe-silicate films on Ru(0001) undergo a spontaneous phase separation into Fe- and Si-rich layers.[15] Perovskite $FeTiO_3$ films can be formed upon Fe depositions onto TiO_2(110).[16] And finally, unique Ba-Ti mixed oxide films with quasi-crystalline structure were successfully synthesized on Au and Pt substrates.[17,18] The specific building principles of 2D mixed oxides were intensively studied also by density functional theory (DFT).[19,20] Hereby, internal electron transfer between the oxide cations was found to be a main trigger for oxide alloying and largely governs the thermodynamic stability of the resulting mixed oxide phase. In a recent work, the formation principles of mixed $V_{2-x}Fe_xO_3$ honeycomb oxides grown on Pt(111) were studied with scanning tunneling microscopy (STM), DFT and Monte Carlo simulations.[21] At moderate temperature, the V and Fe atoms are miscible in the honeycomb lattice for Fe concentrations up to 50%. Driving force is hereby the large thermodynamic stability of V-O-Fe mixed cation pairs with respect to mono-elemental Fe-O-Fe and V-O-V units.

Also the present manuscript deals with V/Fe mixing in a 2D oxide film, with the sole difference that the Pt(111) support used before[21] has been replaced with Ru(0001). Although both substrates share similar lattice parameters and the same hexagonal symmetry, oxide alloying on the Ru surface follows an effec-

tive self-organization scheme that only allows for V to Fe mixing ratios close to 50%. Any deviation from this composition leads to a phase separation into mixed oxide patches and bilayer FeO or VO_x islands in the case of iron or vanadium excess. Our DFT calculations unravels the building principles of the mixed phase, demonstrating how metal/oxide interactions determine cationic mixing in 2D oxide layers.

2. Experiments and Theory

The experiments were carried out in an ultrahigh-vacuum chamber ($p \sim 2\times10^{-10}$ mbar), comprising a liquid-nitrogen cooled STM, a setup for low-energy electron diffraction (LEED) and common surface-science tools for sample cleaning and thin-film preparation. Chemical characterization of the samples was realized by photoelectron spectroscopy (XPS) performed in a second vacuum chamber, being linked to the first one via vacuum transport. STM data acquisition was performed in the constant current mode with electrochemically etched gold tips. The local density of states (LDOS) of the sample was probed with STM conductance spectroscopy using a lock-in amplifier.

The mixed oxide films were grown on a Ru(0001) support, cleaned by Ar^+ sputtering, oxygen annealing and vacuum flashing to 1200 K. In a first preparation step, ~0.5 ML Fe was deposited by electron-beam evaporation onto the substrate held at 700 K. Subsequently, ~0.5 ML V was added at similar temperature, yet in 5×10^{-7} mbar oxygen. The preparation was finalized with a 750 K annealing step, first in O_2 (10 min) and then in vacuum (10 min). The overall sample quality was checked with LEED, whereby sharp (2×2) superstructure spots gave a first hint at a successful synthesis of crystalline V/Fe mixed oxide films. In case of Fe excess during growth, an additional Moiré pattern became visible around the Ru(1×1) spots, indicating the formation of FeO bilayer islands.[22,23,24] Conversely, a V-rich preparation resulted in a complex (4×4) LEED pattern, representing a $\sqrt{48}$ VO_x phase.[25] To determine the exact film composition, i.e. the nature and abundance of binary and ternary oxide contributions, STM measurements were carried out, as presented in chapter 3.

DFT calculations were performed with the Vienna Ab-initio Simulation Package (VASP),[26,27] using the Projector Augmented Wave method[28,29] to represent the electron-core interaction and a 400 eV energy cutoff in the development of Kohn-Sham orbitals on a plane-wave basis set. A dispersion-corrected exchange-correlation functional (optB88-vdW)[30,31,32] was employed within the DFT+U approach proposed by Dudarev.[33,34] As in our previous studies,[35,36,37,38] we utilized U values close to those reported in the literature: U = 1.7 eV for V and U = 3.0 eV for Fe in the sesquioxides. All calculations were spin-polarized and the relative stability of nonmagnetic versus magnetic solutions with either parallel or antiparallel spin moments was systematically tested. Ionic charges were estimated with the partition scheme proposed by Bader,[39,40] and magnetic moments were obtained by integration of the spin density within the Bader vol-

umes. The Tersoff-Hamann approximation was used for STM image simulations,[41] and atomic configurations were plotted with VESTA.[42]

We have considered pure VO_x, FeO_x and mixed $VFeO_x$ layers in a (4×4)-Ru(0001) unit cell at the experimental in-plane bulk lattice parameter (2.705 Å). Sampling of the Brillouin zone was performed with a Γ-centered (2×2×1) Monkhorst-Pack mesh.[43] The Ru substrate was represented by a slab composed of four (111) atomic planes. We checked that adding a 5th metal layer only resulted in negligible corrections on the reported quantities. The oxide film was deposited on one side of the slab and dipole corrections were applied. The atomic coordinates of all anions, cations and Ru atoms in the surface layer were allowed to relax until forces dropped below 0.01 eV Å^{-1}. Apart from the bottom layer that was kept in its bulk position, atoms in the remaining metal layers were allowed to relax only perpendicular to the surface. All formation energies, E_{form} per cation, were calculated with respect to the most stable bulk iron- and vanadium-oxide phase that is corundum Fe_2O_3 and rutile VO_2 at the present experimental conditions ($\Delta\mu_O \sim -1.6$ eV), according to:

$$E_{form} = \frac{1}{(i+j)}\left[E\left(V_iFe_jO_k/Ru\right) - \mathrm{E(Ru)} - \mathrm{i}\cdot\mathrm{E}(VO_2) - \frac{\mathrm{j}}{2}\cdot\mathrm{E}(Fe_2O_3) - (k-2i-1.5j)\left(\frac{1}{2}\mathrm{E}(O_2) - \Delta\mu_O\right)\right]$$

Here, $E(V_iFe_jO_k/Ru)$, E(Ru), $E(VO_2)$, $E(Fe_2O_3)$, and $E(O_2)$ refer to the energies of the supported film, the Ru substrate, one formula unit of bulk VO_2 and bulk Fe_2O_3 and one oxygen molecule, respectively.

3. Experimental results

3.1 Film morphology and strain relaxation

Figure 1a depicts a wide-scale STM image of Ru(0001) taken after reactive V and Fe deposition with a 40:60 ratio. Three surface regions are discernable. The primary phase is a (2×2) V/Fe mixed oxide that homogenously covers the wide terrace at the left. The small regions at the lower right depict FeO bilayer islands, easily distinguished by their unique Moiré pattern with 22 Å periodicity. The upper right region finally reflects the O(2×1)-covered Ru support that is sprinkled with a few V and Fe atoms. Taking the O-covered Ru(0001) as reference, the mixed oxide has an apparent height of 2.9-3.0 Å, while the FeO bilayer protrudes the support by 4.75 Å. The measured heights are nearly independent of bias voltage, indicating their topographic and not electronic origin. As the bilayer FeO,[22,23] and even more the O/Ru(0001) adsorption pattern[44,45] are well described in the literature, they will not be discussed here any further.

When zooming into the V/Fe mixed oxide phase, a partially ordered relaxation network becomes visible at first glance (Fig. 1b). It is made of hexagonal units of 35-40 Å diameter, being filled with a (2×2) pattern of dark minima. Closer inspection reveals that the (2×2) units actually comprise the six-cation rings of a

honeycomb lattice, as detailed in the next section. The hexagonal (2×2) domains are delimited by characteristic grain boundaries, composed of a regular sequence of nine, eight and five-membered rings (Fig. 1c). They follow the well explored boundary scheme of planar hexagonal lattices, as revealed for many van der Waals materials including graphene,[46] and oxide monolayers with honeycomb structure.[47] In the present case, the straight boundary sections exhibit a (558) di-vacancy structure, in which a central octagonal ring is bordered by two pentagonal rings at each side (Fig. 1d). At the corner positions, the octagons are replaced by nine-membered rings that are delimited by six pentagons and three hexagons in order to satisfy the threefold symmetry of the boundary joint. The formation of nine-membered rings is intrinsically connected to the hexagonal shape of the oxide domains and not found for straight boundaries in transition metal dichalcogenide and graphene layers.

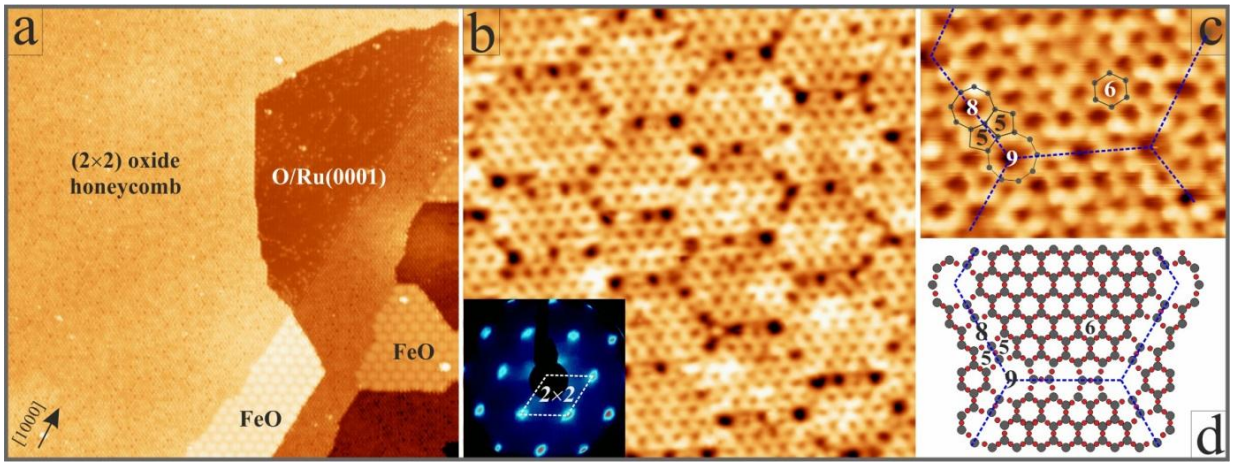

Figure 1: (a) STM overview image of the Ru(0001) surface after reactive Fe and V deposition (75×75 nm^2, U_B = 1.0 V, I = 0.1 nA). **(b)** Relaxation pattern of the V/Fe mixed honeycomb oxide (15×15 nm^2, U_B = -1.5 V). **(c)** Atomically resolved grain boundaries between adjacent oxide domains (5.5×4.2 nm^2, U_B = -0.2 V) and **(d)** corresponding structure model with typical ring sizes being marked (cations: grey, anions: red). The inset in (b) depicts a LEED pattern acquired with 70 eV kinetic energy.

The regular domain structure observed here finds its origin in the lattice mismatch between the mixed honeycomb oxide and the Ru(0001). The (2×2) registry imposed by the substrate puts the oxide lattice under high compressive strain and enables occupation of optimal binding sites only in the domain center. With increasing distance, the interfacial binding positions become unfavorable, and a dislocation line gets inserted after typically three honeycomb rings. The strain release takes place as the (558) ring configuration at the boundary takes less space than the Ru unit cells below. An integer number of overarched Ru unit cells (displacement vector $4a_1+a_2$) hereby ensures that the metal-oxide registry does not change across the boundary line and identical binding sites are occupied in adjacent domains. The hexagonal domain structure thus represents an effective means of strain relaxation in the oxide film.[47,48]

3.2 Atomic structure of the oxide film

High resolution STM images allow for a comprehensive atomic-scale exploration of the mixed honeycomb oxide, generating starting information for our DFT analysis (Fig. 2). At small positive bias, as typically used to resolve the cationic lattice, the six corner cations and the pores of the regular honeycomb rings are detected (Fig. 2b). Distinct triple protrusions and individual rings with elevated contrast already hint at characteristic defects in the oxide film. With increasing bias, three of the six corner cations gain contrast with respect to their neighbors, while the pores become invisible. The result is a distinct (2×2) surface pattern, in which every second cation appears bright (Fig. 2a). This (2×2) network also governs the LEED data shown in the inset of Fig. 1b. At negative polarity, the anion lattice is resolved (Fig. 2c). In correspondence to a honeycomb structure of cations, the anions form a Kagome lattice. The O ions hereby arrange in characteristic triple units, being grouped around the protruding cations of the (2×2) lattice. Every O triple can be associated with a distinct tilt angle, suggesting that rotating the MO_3 units is another means to compensate lattice strain due to the Ru(0001) support (Fig. 2d). Not surprisingly, pronounced perturbations in the anion lattice occur along the domain boundaries.

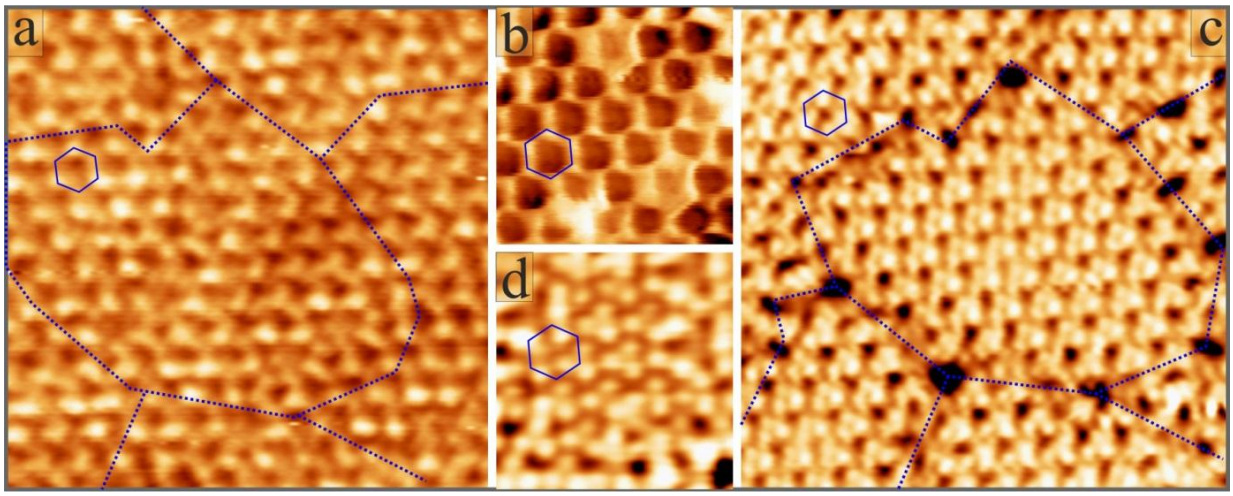

Figure 2: (a) STM image of the cation lattice of the V/Fe mixed honeycomb oxide on Ru(0001) (7×7 nm^2, U_B = 1.0 V, I = 0.5 nA). **(b)** Cation lattice at lower bias voltage (3×3 nm^2, U_B = 0.1 V). **(c)** Anions in the V/Fe mixed honeycomb oxide forming a Kagome lattice (7×7 nm^2, U_B = -1.5 V, I = 1.0 nA). **(d)** Zoom into the anion lattice (3×3 nm^2, U_B = -0.1 V). Grain boundaries between neighboring oxide domains are highlighted by dashed lines. Blue hexagons mark the (2×2) unit cell of the oxide film.

3.3 Atomic-scale defects in the oxide film

Besides line defects, two characteristic point defects can be distinguished in the mixed honeycomb lattice. Their individual fingerprints become evident in polarity and bias-dependent STM data, as depicted in Fig. 3. Type I defects are seen best at low positive bias, when they show up as distinct shamrock units localized at the contact point of three honeycomb rings (Fig. 3a, triangular markers). With increasing bias, the three (2×2) cations next to the defect turn bright, while the actual defect center is not detected anymore (Fig. 3b, top). The apparent height of this defect-related triplet reaches a maximum of 60 pm with respect

to regular 2×2 maxima at 0.5 V, decreasing again at higher bias. Type I defects are also seen at negative polarity, when they are governed by three MO_3 units with particularly high contrast (Fig. 3b, bottom). All type I defects retain their orientation when crossing a dislocation line in the film, reflecting the identical metal-oxide registry in all oxide domains. Only when moving to an adjacent Ru(0001) terrace, the type I defects rotate by 180° in correspondence to the ABAB stacking of hcp ruthenium.

Type II defects show up as single honeycomb rings with enhanced contrast at sample voltages close to the Fermi level (E_F) (Fig. 3a, round markers). With increasing bias, the three (2×2) cations surrounding the anomalous rings gain intensity with respect to their neighbors, producing again shamrock-type maxima (Fig. 3c, top). However, these triplets have an inverted orientation with respect to type I defects, as they are centered at a honeycomb ring and not at the contact point of three rings. At negative polarity, the regular arrangement of MO_3 units changes into a quasi-triangular atomic pattern around type II defects (Fig. 3c, bottom). Closer inspection reveals that the Kagome O lattice prevails also in these areas; however, the anions in the middle of the triangles appear with reduced contrast. Unique for all type II defects is a continuously increasing height at rising positive bias, until they surmount the oxide surface by more than 1 Å at 3.0 V (Fig. 3a). Simultaneously, their appearance evolves to a single protrusion located in the ring center, as compared to the low-bias shamrock shape. Similar to type I defects, the orientation of type II defects inverts when moving from one to the next Ru terrace, but not when crossing a domain boundary.

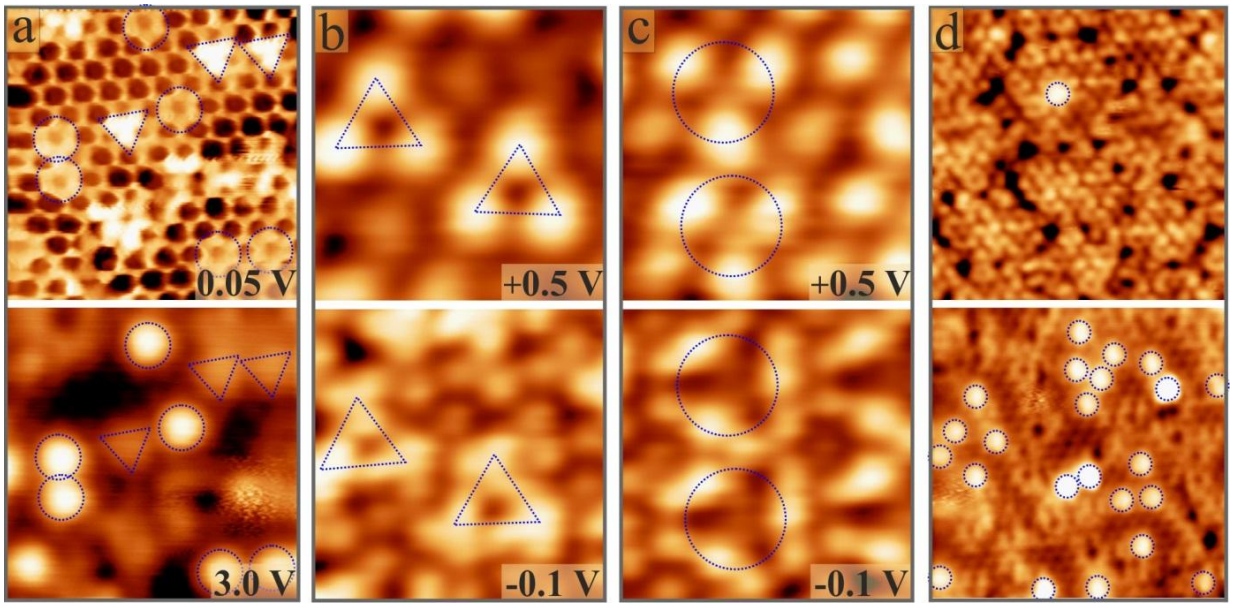

Figure 3: (a) Bias-dependent contrast of type I (blue triangles) and type II (blue circles) defects in V/Fe mixed honeycomb oxides (7×7 nm^2, I = 0.5 nA). Close up-images of **(b)** type I and **(c)** type II defects at positive and negative polarity (3×3 nm^2). The defects locate at the same Ru(0001) terraces, and are oriented in opposite direction. **(d)** STM image of a nearly stoichiometric V/Fe (top) and a Fe-rich (bottom) mixed honeycomb oxide, taken at 3.0 V sample bias to maximizes the contrast of type II defects (11×11 nm^2).

The abundance of point defects in the mixed honeycomb oxides depends on the preparation conditions, for example the V/Fe ratio during deposition. In particular, the concentration of type II defects, readily detected by their bright high-bias contrast, increases with Fe concentration in the film. Whereas the nearly stoichiometric sample shown in the top panel of Fig. 3d contains ~1×10^{12} cm^{-2} type II defects, the concentration rises to 2×10^{13} cm^{-2} in the bottom film that has been prepared in Fe excess. The nature of the point defects is analyzed by DFT calculations, being discussed in the next section. We note that additional information on the film composition has been derived from STM conductance and XP spectroscopy, as shown in the supporting information (Figs. S1 and S2).

4. Theoretical results

4.1. Structure and electronic properties of V/Fe mixed oxide films

In a first step, we have modelled supported oxide films with a 6-cation ring structure and a V/Fe cation ratio of 1 to 1. More precisely, starting from the simplest mixed $VFeO_3$ honeycomb film directly deposited on the Ru surface, we have constructed a series of $VFeO_n$ (n = 4-7) configurations by successive addition of oxygen. Different configurations have been considered for each stoichiometry, with O atoms added either on top of the oxide film or at the Ru/oxide interface. In the latter case, various offsets between the Ru substrate, the interfacial oxygens, and the oxide layer have been tested. Fig. 4a summarizes the formation energies of the lowest energy configurations at each oxygen content as a function of the oxygen chemical potential. The respective atomic structures are reported in the SI, Fig. S3.

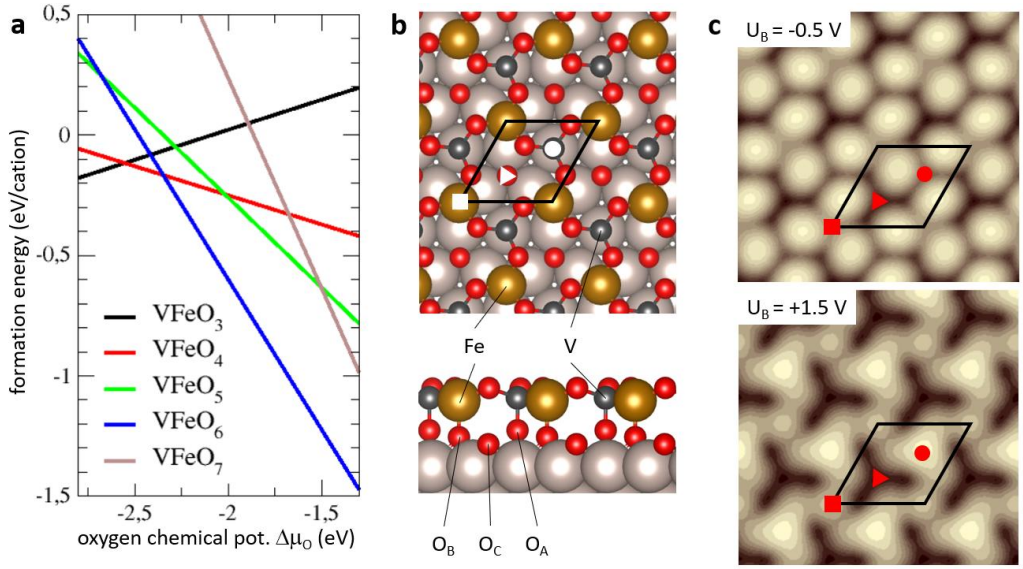

Figure 4. (a) Formation energies of Ru-supported mixed $VFeO_n$ honeycomb films with various oxygen contents, n = 3-7, as a function of oxygen chemical potential, referred to the corresponding bulk VO_2 and Fe_2O_3 phases. **(b)** Top

and side views of the most stable $VFeO_6$ film. Three inequivalent interfacial oxygen atoms O_A, O_B, and O_C as well as the (4×4)-Ru(0001) surface unit cell are indicated. Golden, red and grey balls represent Fe, O and V atoms, respectively. **(c)** Simulated STM images at negative (U_B = -0.5 V) and positive (U_B = +1.5 V) sample bias with circle, square, and triangle marking the positions of the O_A, O_B, and O_C sites.

We find that the O-rich $VFeO_6$ film is by far the most stable among all considered structures around the experimental oxygen conditions ($\Delta\mu_O \sim -1.6$ eV). The $VFeO_3$ honeycomb film becomes favored only in an extremely O-poor environment ($\Delta\mu_O$ < -2.5 eV), while films with either intermediate ($VFeO_4$ and $VFeO_5$) or high O content ($VFeO_7$) are not stable in the considered range of chemical potentials. The most stable $VFeO_6$ film, Fig. 4b, can be seen as a $VFeO_3$ honeycomb layer linked to the Ru(0001) substrate by three interfacial oxygen atoms, positioned either in top (O_A) or hollow sites of the Ru surface (O_B and O_C). While O_A and O_B atoms form bonds with V and Fe cations, respectively, O_C has no link to the $VFeO_3$ layer and provides an open adsorption site in the center of the honeycomb rings to be used for film functionalization. The electronic characteristics of the $VFeO_6$ film are consistent with its large oxygen content. The LDOS, Bader charges and magnetic moments (see SI, Fig. S4 and Tab. S1) concomitantly provide a clear signature of V^{5+} and Fe^{3+} formal oxidation states. Such large formal charges result from an electron transfer to the interfacial oxygen atoms O_A and O_B, the Bader charges of which are noticeably larger than the O_C charge. As discussed in the SI, the $VFeO_6$ film can be considered as a charge-neutral $V^{5+}Fe^{3+}O^{-2}{}_4$ layer deposited on an O-covered Ru surface, with two such O atoms per $VFeO_4$ formula unit.

The simulated STM contrast of the $VFeO_6$ film, Fig. 4c, is in good agreement with the experimental signature. Directly below E_F, where the LDOS of all film ions is relatively small (Fig. S4), the contrast is governed by the oxygens in the oxide layer that relax outward by 0.5 Å with respect to the V and Fe ions and therefore produce the Kagome lattice seen at negative bias. Conversely, the LDOS above E_F is dominated by cation contributions. At U_B = +1.5 V, the V sites appear much brighter than the Fe sites, despite their lower LDOS, which points to a geometric contrast mechanism again. Indeed, the Fe cations are located 0.15 Å closer to the substrate than the V species, although both cations are 4-fold coordinated with three in-plane ($d_{O\text{-}V}$ = 1.74 Å, $d_{O\text{-}Fe}$ = 1.86 Å) and one out-of-plane ($d_{O\text{-}V}$ = 1.73 Å, $d_{O\text{-}Fe}$ = 1.96 Å) bond. Despite the expanded vertical Fe-O_B bond, the Fe position is lowered due to the strong downward displacement of the hollow-bound O_B with respect to top-bound O_A oxygen. The total calculated height of the $VFeO_6$ film (2.5 Å with respect to the O-covered surface) is about 1 Å larger than that of a simple $VFeO_3$ honeycomb film. It coincides very well with the experimental estimate and unambiguously supports the presence of interfacial oxygen atoms.

4.2. Signature of point defects in the V/Fe mixed oxide films

As to identify the experimentally observed defects in the mixed film, we have systematically simulated V and Fe substitutions (sub) and interstitials (int), as well as oxygen vacancies and ad-atoms in a (4×4)-Ru (0001) cell and compared their calculated signatures with the STM data. In the case of substitutions, i.e. a V cation replaces a Fe on an O_B site or a Fe cation replaces a V on an O_A site, we find a dominant contrast for cations in the O_A sites in positive-bias STM simulations, while cations in O_B sites are systematically less visible. This is illustrated by the diminished contrast of V_{sub} on an O_B site as compared to the same cation on O_A, and by the bright Fe_{sub} atom on an O_A site that even exceeds the contrast of the original V cations at this position (SI, Fig. S5). Regarding V or Fe interstitials, i.e. additional V or Fe cations bound to an O_C oxygen in the ring center, we find an overall weak contribution to the STM contrast as compared to cations on the O_A sites. Our computational results thus confirm that only half of the cations in the mixed honeycomb film is visible in the STM, as the positive-bias contrast is systematically driven by cations bound to O_A sites. Consequently, only very limited information can be obtained from STM images on the nature of cations located on O_B sites and on the presence and type of cations on O_C sites. However, a reliable assignment of the two defect types may still be achieved from bias-dependent STM images.

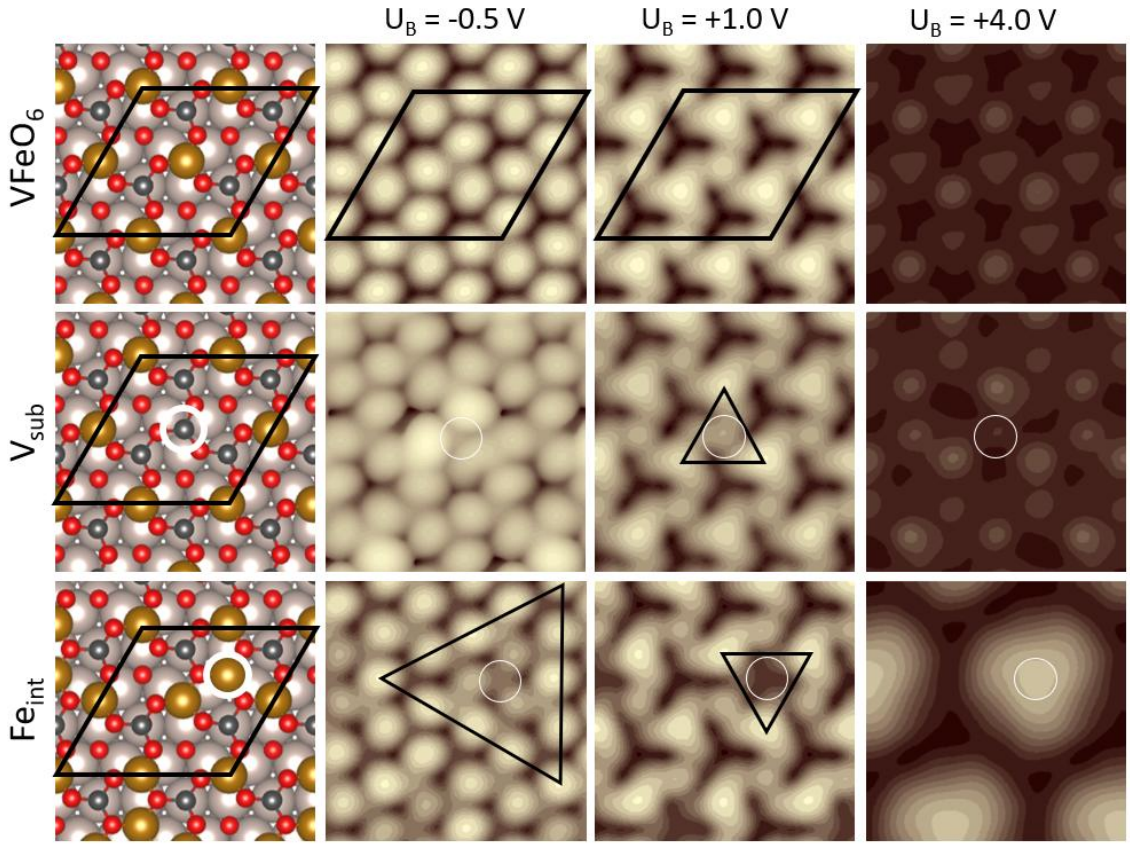

Figure 5: Structural models and simulated STM images of the perfect $VFeO_6$ film (top), a V substitution (middle), and an Fe interstitial (bottom) as a function of bias U_B = -0.5 V, +1.5 V, and +4.0 V. Positions of defects are indicated with white circles and characteristic motifs are highlighted with black triangles. The (4×4) surface unit cell is also indicated.

Regarding type I defects, their experimentally determined localization at the vortex of three adjacent honeycomb rings with no contrast in the perfect lattice suggests a point defect on an O_B site (Fig 3b). Since the O_B sites are less accessible to STM, the point defect itself produces only a weak contrast change but enhances the contrast of the three neighboring O_A-type cations. We find that a V_{sub} cation produces an STM signature consistent with the experimental observations: (i) it hardly modifies the Kagome pattern observed at negative polarity, (ii) it enhances the contrast at neighboring O_A sites at moderate positive bias, and (iii) its effect vanishes at higher bias voltage (Fig. 5, middle row). In contrast, type II defects that are localized in the center of honeycomb rings produce a pronounced STM signature at both negative and positive polarity. The best match between calculated and experimental STM signature (Fig. 3c) is hereby obtained for an interstitial Fe_{int} cation that displays: (i) a large triangular pattern at negative bias; (ii) a shamrock-type pattern similar yet mirrored to that of type I defects at moderate positive bias; and (iii) a single protruding feature of 1 Å apparent height in the ring center at high positive bias (Fig. 5, lower row). In the forthcoming discussion, we will show that the above assignment is further supported by the favorable stability of these two point-defects in mixed V/Fe honeycomb films.

5. Discussion

In this section, the construction principle and thermodynamic stability of the mixed $VFeO_6$/Ru phase will be addressed. Its atomic structure consists of an alternating arrangement of V and Fe cations in six-membered rings, with vanadium bound to interfacial O_A anions and iron to O_B sites. We find that this cationic arrangement is by far the most stable. On the one hand, the mixed configuration in which all V and Fe cations exchange sites is less stable by ~0.4 eV per cation pair. This reveals a significant site effect which can be explained by V-$O_{A,B}$ bond strengths larger than Fe-$O_{A,B}$ ones. Indeed, the cost of interfacial oxygen-vacancy formation is systematically 1 eV larger for V-O pairs regardless the site. As a result, as the cation-O_B bond lengths is intrinsically expanded due to the lower topographic height of O_B compared to O_A anions, the associated energy cost is lower in the V-O_A/Fe-O_B than in the reverse atom arrangement. Moreover, all other cation configurations that necessarily involve V-V and Fe-Fe cation pairs exhibit higher energies as well. Apart from the site effect, there is an additional energy cost of ~0.6 eV for creating V-V and Fe-Fe first neighbor pairs in place of two V-Fe ones. This provides a strong energetic bias for the formation of mixed cation pairs, in which pure electrostatic interactions are expected to play the major role. Given the different charge state of cations in the honeycomb lattice, replacing two mixed Fe^{3+}–V^{5+} pairs by one Fe^{3+}–Fe^{3+} and one V^{5+}–V^{5+} is highly unfavorable from an electrostatic point of view.

Beyond the 50% composition, Figure 6a shows that substitutions and interstitials of either V or Fe cations into the honeycomb lattice reduce the film stability. The destabilization is relatively weak for isolated V

substitutions that correspond to the type I defects observed experimentally, while formation of V interstitials is energetically more expensive. In contrast, the destabilizing effect of isolated Fe interstitials (type II defects in the STM images) and substitutions is more pronounced. Further substitutions keep increasing the energy and eventually lead to iso-structural V_2O_6 and Fe_2O_6 end-members with especially high formation energies (dashed red lines in Fig. 6a). These end-members turn out to be much less stable than alternative models of binary oxide structures that we have constructed on (4×4) unit cells of Ru(0001): a V_5O_{21} layer consisting of large 12-cation rings reminiscent of the recently reported √48 phase (Fig. 6b),[25] and a FeO_2 film, consisting of small 3-cation rings that is similar to FeO(111)-like phases reported in the literature (Fig.6c).[22,23,24] The $VFeO_6$ phase thus represents a compromise between the two binary oxide parents in terms of structure (ring size) and oxygen stoichiometry.

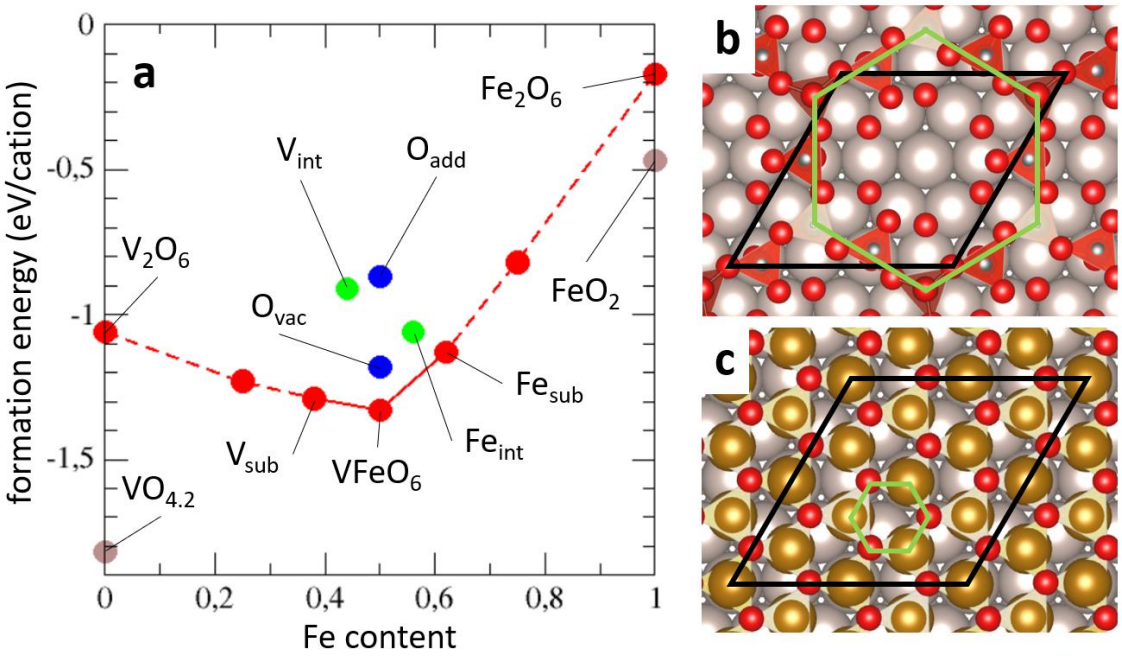

Figure 6: **(a)** Formation energy of the mixed $VFeO_6$ phase, either pristine or with substitutional, interstitial, and vacancy defects, as a function of the Fe content and at the experimental oxygen conditions ($\Delta\mu_O = -1.6$ eV). The values for pure vanadium and iron oxide model structures are indicated by brown dots and top views of the respective lattices are shown in **(b)** and **(c)**.

The mixed $VFeO_6$ layer with its unique composition and structure, being so different from the parent vanadium and iron oxide layers, complies with a general scenario of mixing well referenced in bulk oxides. Indeed, beyond the doping regime, mixing two oxides with different structure and stoichiometry may lead either to phase separation, as in ZnO-MgO,[49] or to the formation of one (or several) mixed compound with distinct structural and compositional characteristics. Silicate compounds, among others, illustrate the latter case and mixing of MgO or FeO with SiO_2 may result in Mg_2SiO_4 or Fe_2SiO_4 crystals with forsterite structure, or perovskite $MgSiO_3$ or $FeSiO_3$. These two families of structures have a different cation-to-cation

ratio and a different oxygen stoichiometry, but they both assure global charge neutrality and an optimal connectivity of the octahedral Mg^{2+} (Fe^{2+}) and tetrahedral Si^{4+} environment. Similarly, in two dimensions, the most stable mixed $VFeO_6$ phase on Ru(0001) displays a self-organization scheme which tolerates only compositions close to 50%. At this point it is worth noting that this mixed 2D phase obeys Pauling's second rule.[50] It states that the charge of each anion compensates the strength V/Z of the valence bond to an adjacent cation (V and Z for cationic valence and coordination number, respectively). While this rule is strictly followed in favorable V-Fe mixed pairs in $VFeO_6$, it is not obeyed by O ions bridging either V-V or Fe-Fe pairs, leading to a local charge imbalance and higher DFT formation energies.

Finally, while both the present $VFeO_6$/Ru(0001) and the recently reported family of $V_{2-x}Fe_xO_3$/Pt(111) films were synthetized at similar experimental conditions and display a comparably strong driving force for cationic mixing, the microscopic effects involved in the stabilization of the mixed phase are qualitatively different. Most importantly, the flexibility of electron transfer toward the electronegative Pt substrate allows the V cations to preserve high oxidation states for all V/Fe ratios up to x=1, resulting in various composition-specific cation distribution patterns (chains, rings, triangles).[21] In contrast, the O(2×1)-Ru(0001) substrate appears more rigid from an electronic point of view. It exhibits 70% less charge variability than Pt in the same range of V/Fe ratios. This dramatically reduces the number of stable film compositions and is responsible for a mixing scenario closer to that met in 3D oxides.

6. Conclusion

We report the successful synthesis and characterization of a mixed oxide phase on the Ru(0001) surface, which displays a highly effective self-organization scheme that tolerates only V:Fe compositions close to 50%. High resolution STM imaging reveals a honeycomb structure of six-membered cation rings, which deviates distinctively from the pure iron and vanadium oxide films obtained under the same experimental conditions. The large apparent height of the film suggests the presence of interfacial oxygen below the mixed oxide layer, consistent with the starting O(2×1)-Ru(0001) surface structure. Dedicated DFT calculations rationalized the experimental findings, clarified the energetic aspect, and revealed structural details complementary to the experiment, in particular, the inequality of the two cationic sites and a strong preference for V atoms to occupy only one of them (site O_A). Moreover, despite the fact that only the protruding cations in O_A sites produce bright STM contrast, the analysis of bias-dependent data enabled a convincing assignment of the two defect types observed experimentally.

The DFT results also demonstrated the remarkable stability of the mixed cation arrangement in $VFeO_6$ films, which relates to a strong site effect and electrostatic interactions, both favoring mixed cationic pairs.

Moreover, the unique structure and stoichiometry of the $VFeO_6$ layer, being intermediate between those of the pure vanadium and iron oxide layers at the same experimental conditions, indicate a 2D mixing scenario that is reminiscent of the one known for mixed bulk oxides. Comparison with the V/Fe oxide films previously synthesized on Pt(111) emphasizes the key role of interfacial O atoms for cationic mixing, further improving our understanding of fundamental principles of oxide alloying in 2D.

ASSOCIATED CONTENT

The Supporting Information is available free of charge at https://pubs.acs.org/doi/

1. STM conductance spectroscopy data
2. XPS results
3. DFT atomic structures
4. DFT electronic structures
5. Simulated STM signatures of point defects

Corresponding authors:

- J. Goniakowski - CNRS-Sorbonne Université, UMR 7588, INSP, F-75005 Paris, France http://orcid.org/0000-0003-4647-9566; email: jacek.goniakowski@insp.jussieu.fr
- N. Nilius - Institut für Physik, Carl von Ossietzky Universität, D-26111 Oldenburg, Germany http://orcid.org/0000-0003-0264-120X; email: niklas.nilius@uni-oldenburg.de

Notes

The authors declare no competing financial interest.

Acknowledgements

Financial support from the DFG grant Ni 650-5/2 '*Functionalization of Cuprous Oxide: From Tailoring the Optical Response to Cu-based Ternary Oxide Materials'* is gratefully acknowledged.

Reference List

[1] McFarland, E. W.; Metiu, H. Catalysis by Doped Oxides, *Chem. Rev.* **2013,** *113*, 4391-4427.

[2] Soldat, J.; Marschall, R.; Wark, M. Improved Overall Water Splitting with Barium Tantalate Mixed Oxide Composites. *Chem. Sci.* **2014**, *5*, 3746–3752.

[3] Wang, S. B.; Hou, Y. D.; Wang, X. C. Development of a Stable $MnCo_2O_4$ Cocatalyst for Photocatalytic CO_2 Reduction with Visible Light, *Appl. Mat. Interfaces* **2015,** *7*, 4327-4335.

[4] Wang, G. P.; Zhang, L.; Zhang, J. J. A review of electrode materials for electrochemical supercapacitors, *Chem. Soc. Rev*. **2012,** *41*, 797-828.

[5] Pauling, L. The principles determining the structure of complex ionic crystals. *J. Am. Chem. Soc.* **1929**, *51*, 1010-1026.

[6] Pena, M. A.; Fierro, J. L. G. Chemical structures and performance of perovskite oxides, *Chem. Rev.* **2001**, *101*, 1981-2017

[7] Zhao, Q.; Yan, Z. H.; Chen, C. C.; Chen, J. Spinels: Controlled Preparation, Oxygen Reduction/Evolution Reaction Application, and Beyond, *Chem. Rev.* **2017,** *117*, 10121-10211.

[8] Chhowalla, M.; Shin, H. S.; Eda, G.; Li, L. J.; Loh, K. P.; Zhang, H. The chemistry of two-dimensional layered transition metal dichalcogenide nanosheets, *Nat. Chem.* **2013**, *5*, 263-275.

[9] Lichtenstein, L.; Heyde, M.; Ulrich, S.; Nilius, N.; Freund, H.-J. Probing the properties of metal-oxide interfaces: Silica films on Mo and Ru supports, *J. Phys.: Condens. Matter* **2012,** *24*, 354010.

[10] Nilius, N.; Freund, H. J. Activating Nonreducible Oxides via Doping, Acc. Chem. Res. **2015.** *48*, 1532-1539.

[11] Sun, Z.; Rodríguez-Fernández, J.; Lauritsen, J. V. Water Dissociation on Mixed Co–Fe Oxide Bilayer Nanoislands on Au(111). *J. Phys. Condens. Matter* **2022**, *34*, 164004.

[12] Pomp, S.; Kuhness, D.; Barcaro, G.; Sementa, L.; Mankad, V.; Fortunelli, A.; Sterrer, M.; Netzer, F. P.; Surnev, S. Two-Dimensional Iron Tungstate: A Ternary Oxide Layer with Honeycomb Geometry. *J. Phys. Chem. C* **2016**, *120*, 7629–7638.

[13] Mohammadi, M.; Negreiros, F. R.; Radlinger, T.; Edelmayer, P.; Netzer, F. P.; Surnev, S. Interaction of Na with 2D WO_3 and MoO_3 Layers on Pd(100): From Doping to 2D Bronze Formation, *J. Phys. Chem. C* **2022,** *126*, 3289-3300.

[14] Lockhorn, M.; Kasten, P. E.; Tosoni, S.; Pacchioni, G.; Nilius, N. Growth and characterization of Ca-Mo mixed oxide films on Mo(001), *J. Chem. Phys.* **2019,** *151*, 234708.

[15] Włodarczyk, R.; Sauer, J.; Yu, X.; Boscoboinik, J. A.; Yang, B.; Shaikhutdinov, S.; Freund, H. J. Atomic Structure of Ultrathin Fe-Silicate Films on a Metal: A Monolayer of Clay? *J. Am. Chem. Soc.* **2013**, *135*, 19222–19228.

[16] Halpegamage, S.; Ding, P.; Gong, X.; Batzill, M. Ordered $FeTiO_3$ Mixed Monolayer Oxides on TiO_2(110). *ACS Nano* **2015**, *9*, 8627–8636.

[17] Forster, S.; Meinel, K.; Hammer, R.; Trautmann, M.; Widdra, W. Quasicrystalline structure formation in a classical crystalline thin-film system, *Nature* **2013,** *502*, 215-218.

[18] Wu, C.; Castell, M. R.; Goniakowski, J.; Noguera, C. Stoichiometry engineering of ternary oxide ultrathin films: $Ba_xTi_2O_3$ on Au(111). *Phys. Rev. B* **2015**, *91*, 155424.

[19] Goniakowski, J.; Noguera, C. Intrinsic Properties of Pure and Mixed Monolayer Oxides in the Honeycomb Structure: M2O3 and MM′O3 (M, M′ = Ti, V, Cr, Fe). *J. Phys. Chem. C* **2019**, *123*, 7898–7910.

[20] Goniakowski, J.; Noguera, C. Properties of Metal-Supported Oxide Honeycomb Monolayers : M_2O_3 and MMO_3 on Me(111) (M , M = Ti , V , Cr , Fe ; Me = Ag , Au , Pt). *J. Phys. Chem. C* **2020**, *124*, 8186–8197.

[21] Wemhoff, P. I..; Nilius, N.; Noguera, C.; Goniakowski, J. Two-Dimensional Oxide Alloys Probed at the Atomic Level: $(V,Fe)_2O_3$ Honeycomb Monolayers on Pt(111), *J. Phys. Chem*. C **2022**, *126*, 5070–5078.

[22] Ketteler, G.; Ranke, W. Heteroepitaxial growth and nucleation of iron oxide films on Ru(0001), *J. Phys. Chem*. B **2003**, *107*, 4320-4333.

[23] Palacio, I.; Monti, M.; Marco, J. F.; McCarty, K. F.; de la Figuera, J. Initial stages of FeO growth on Ru(0001), *J. Phys.: Condens. Matter* **2013,** *25*, 484001.

[24] Ossowski, T.; Wang, Y.; Carraro, G.; Kiejna, A.; Lewandowski, M. Structure of Mono- and Bilayer FeO on Ru(0001): STM and DFT Study. *J. Magn. Magn. Mater.* **2022**, *546*. 168832.

[25] Wang, Y.; Wemhoff, P. I.; Lewandowski, M.; Nilius, N. Electron stimulated desorption of vanadyl-groups from vanadium oxide thin films on Ru(0001) probed with STM, *Phys. Chem. Chem. Phys* **2021,** *23*, 8439- 8445.

[26] Kresse, G.; Hafner, J. Ab initio molecular dynamics for liquid metals. *Phys. Rev.* B **1993**, *47*, 558−561.

[27] Kresse, G.; Furthmuller, J. Efficient iterative schemes for ab initio total energy calculations using a plane-wave basis set. *Phys. Rev.* B **1996**, *54*, 11169−11186.

[28] Blöchl, P. E. Projector augmented-wave method. *Phys. Rev.* B **1994**, *50*, 17953−17979.

[29] Kresse, G.; Joubert, D. From ultrasoft pseudopotentials to the projector augmented-wave method. *Phys. Rev.* B **1999**, *59*, 1758−1775.

[30] Dion, M.; Rydberg, H.; Schroder, E.; Langreth, D. C.; Lundqvist, B. I. Van der Waals density functional for general geometries. *Phys. Rev. Lett*. **2004**, *92*, 246401.

[31] Klimes, J.; Bowler, D. R.; Michaelides, A. Chemical accuracy for the van der Waals density functional. *J. Phys.: Condens. Matter* **2010**, *22*, 022201.

[32] Klimes, J.; Bowler, D. R.; Michaelides, A. Van der Waals density functionals applied to solids. *Phys. Rev.* B **2011**, *83*, 195131.

[33] Anisimov, V. I; Aryasetiawan, F; Lichtenstein, A I First principles calculations of the electronic structure and spectra of strongly correlated systems: the LDA+U method. *J. Phys.: Condens. Matter* **1997**, *9*, 767−808.

[34] Dudarev, S. L.; Botton, G. A.; Savrasov, S. Y.; Humphreys, C. J.; Sutton, A. P. Electron-energy-loss spectra and the structural stability of nickel oxide: An LSDA+U study. *Phys. Rev.* B **1998**, *57*, 1505−1509.

[35] Le, H.-L. T.; Goniakowski, J.; Noguera, C. Properties of mixed transition metal oxides: $MM'O_3$ in corundum-type structures (M, M' = Al, Ti, V, Cr, and Fe). *Phys. Rev. Mater.* **2018**, *2*, 085001.

[36] Goniakowski, J.; Noguera, C. Intrinsic properties of pure and mixed monolayer oxides in the honeycomb structure: M_2O_3 and $MM'O_3$ (M, M' = Ti, V, Cr, Fe). *J. Phys. Chem.* C **2019**, *123*, 7898−7910.

[37] Le, H.-L.; Goniakowski, J.; Noguera, C. 0001 Interfaces between M_2O_3 corundum oxides (M = Al, Ti, V, Cr, Fe). *Surf. Sci.* **2019**, *679*, 17−23.

[38] Goniakowski, J.; Noguera, C. Properties of M_2O_3/Au(111) honeycomb monolayers (M = Sc, Ti, V, Cr, Mn, Fe, Co, Ni). *J. Phys. Chem.* C **2019**, *123*, 9272−9281.

[39] Bader, R. F. W. A quantum theory of molecular structure and its applications. *Chem. Rev.* **1991**, *91*, 893−928.

[40] Henkelman, G.; Arnaldsson, A.; Jonsson, H. A fast and robust algorithm for Bader decomposition of charge density. *Comput. Mater. Sci.* **2006**, *36*, 354−360.

[41] Tersoff, J.; Hamann, D. R. Theory of the scanning tunneling microscope. *Phys. Rev.* B **1985**, *31*, 805.

[42] Momma, K.; Izumi, F. VESTA 3 for three-dimensional visualization of crystal, volumetric and morphology data. *J. Appl. Crystallogr.* **2011**, *44*, 1272−1276.

[43] Monkhorst, H.; Pack, J. Special points for Brillouin-zone integrations. *Phys. Rev.* B **1976**, *13*, 5188−5192.

[44] Piercy, P.; DeBell, K.; Pfnür, H. Phase diagram and critical behavior of the adsorption system 0/Ru(001): Comparison with lattice-gas models, *Phys. Rev. B* **1991,** *45*, 1869.

[45] Nilius, N.; Mitte, M.; Neddermeyer, H. Low-temperature STM study of O_2 adsorption on Ru(0001), *Appl. Phys. A.* **1998,** *66*, 519.

[46] Huang, P. Y.; Ruiz-Vargas, C. S.; Van Der Zande, A. M.; Whitney, W. S.; Levendorf, M. P.; Kevek, J. W.; Garg, S.; Alden, J. S.; Hustedt, C. J.; Zhu, Y.; et al. Grains and Grain Boundaries in Single-Layer Graphene Atomic Patchwork Quilts. *Nature* **2011**, *469*, 389–392.

[47] Wang, S.; Hu, X.; Goniakowski, J.; Noguera, C.; Castell, M. R. Epitaxially Constrained Grain Boundary Structures in an Oxide Honeycomb Monolayer. *Adv. Mater. Interfaces* **2022**, *2102213*, 1–11.

[48] Benedetti, S.; Stavale, F.; Valeri, S.; Noguera, C.; Freund, H.-J.; Goniakowski, J.; Nilius, N. Steering the Growth of Metal Ad-particles via Interface Interactions Between a MgO Thin Film and a Mo Support, *Adv. Funct. Mat*. **2013,** *23*, 75–80

[49] Ohtomo, A; Kawasaki, M.; Sakurai, Y.; Ohkubo, I.; Shiroki, R.; Yoshida, Y.; Yasuda, T.; Segawa, Y.; Koinuma, H. Fabrication of alloys and superlattices based on ZnO towards ultraviolet laser, *Mater. Sci. Eng. B* **1998,** 56, 263–266

[50] Pauling, L. The principles determining the structure of complex ionic crystals. *J. Am. Chem. Soc.* **1929**, *51*, 1010-1026.

TOC Graphic: